ELSEVIER

Contents lists available at ScienceDirect

# **Precision Engineering**

journal homepage: www.elsevier.com/locate/precision





# Machine learning enhanced high dynamic range fringe projection profilometry for in-situ layer-wise surface topography measurement during LPBF additive manufacturing

Haolin Zhang, Chaitanya Krishna Prasad Vallabh, Xiayun Zhao

ZXY Intelligent Precision - Advanced Manufacturing (ZIP-AM) Laboratory, Department of Mechanical Engineering and Materials Science, University of Pittsburgh, Pittsburgh, PA, 15261, USA

### ARTICLE INFO

Handling Editor: Prof. R. Leach

Keywords:
Additive manufacturing
In-situ monitoring
Fringe projection profilometry
High dynamic range
Machine learning
Surface topography
Super resolution

### ABSTRACT

Fringe Projection Profilometry (FPP) is a cost-effective and non-destructive method, typically used for measuring finer features and reconstructing 3D topography of objects. However, to use the FPP method for measuring the dynamic topography of powder bed and printed layers during Laser Powder Bed Fusion (LPBF) based additive manufacturing (AM) process, unique challenges exist due to the varying material properties and ambient conditions in the build chamber. In this work, we aim to enhance the discernibility, accuracy, and resolution of FPP in the specific application scenario of measuring layer-wise surface topography during LPBF AM by integrating our recently developed LPBF-specific FPP sensing model that features localized sensor calibration and Fourier filter-aided unwrapping with an equipment-based High dynamic range (HDR) method and machine learning (ML) aided FPP data analysis. First, a projector based HDR method is applied to mitigate the shadowing and intensity saturation problems by projecting sinusoidal fringe patterns of varying intensities. Secondly, a ML framework is developed to improve the surface topography measurement accuracy (RMSE from 10.57 µm to  $7.49~\mu m$  or even  $4.35~\mu m$  for directly measurable points) and enhance resolution that is currently subjected to hardware limitations (from 38 µm to 5 µm laterally and from 10 µm to 1 µm vertically). Several different types of candidate neural networks (NNs) are trained and tested using the in-situ FPP measurement data and ex-situ standard optical microscopy characterization data. Multiple NN-based models are resulted and compared in terms of their ability to enhance the accuracy and resolution of FPP's end-result (height measurement). By selecting the best-performance NN enabled image super resolution model, the proposed ML integrated HDR FPP method is expected to measure the surface topography of printed layers during LPBF-AM more capably and efficiently, thus advancing the existing state-of-the-art methods towards the desired online inspection of LPBF print defects.

# 1. Introduction

# 1.1. Additive manufacturing and in-situ surface measurement

Laser powder bed fusion (LPBF) based additive manufacturing (AM) processes utilize a laser to sinter or melt thin layers of metal powders for fabricating products with reduced cost and time. These processes have applications in various industries including aerospace, medical, and automobile [1–3]. However, due to certain print defects (such as porosity, surface bumps and voids), the printed parts are often far from being qualified for practical use. Comprehensive process control methods need to be developed and implemented, based on in-situ

monitored process signatures, for manufacturing quality parts. Among all the possible process signatures, surface topography provides essential information about the surface defects such as powder spatter redeposition, lack-of-fusion, balling, voids, and bumps at each print layer, which could be detrimental for part properties. Surface topography in metal AM is strongly influenced by the print process parameters, as they affect the heat dissipation rates and thermal gradients during the print. These variations in the thermal properties cause surface defects, recoater crash, porosity, among other defects [4–6]. Other factors which affect a print part's surface topography include powder reuse, position and orientation on the build platform (overhang structures tend to have rougher surfaces), part interaction with the recoater blade [7].

E-mail address: xiayun.zhao@pitt.edu (X. Zhao).

<sup>\*</sup> Corresponding author.

Numerous methods for evaluating the surface of objects have been implemented, which include stylus-based approaches such as optical profilometry systems [8], phase shifting interferometry [9], confocal microscopy [6], optical coherence tomography (OCT) [10], focus variation microscopy [7] among others. While all these methods are good choices for measuring surface properties for AM parts, they are often limited either by the cost, ease of utilization, in-situ/online process monitoring, or region of interest (ROI) requirements. For instance, OCT systems cannot be implemented online easily and have a typical ROI in the order of  $10 \times 10$  mm which is not optimal for a print process monitoring for larger build areas. However, the spatial resolution of OCT is in order of 10's of microns which is of great interest in characterizing porosity of AM parts. Yet, implementing OTC laser scans across each layer for in-situ surface measurement during AM is slow. For example, it took  $\sim$ 20 s to collect OTC data over an area of 4.4  $\times$  4.4 cm<sup>2</sup> with a pixel resolution of 100 µm during LPBF, necessitating a pause of printing between layers [11]. Similarly, focus variation microscopy also has a good spatial resolution but cannot be implemented for online monitoring.

Further, most of these methods can only measure offline the surface topography of a completed part. However, it has to be noted that the surface quality of the final AM manufactured part quality is dependent on all the print layers [12], thus making each print layer's surface topography monitoring essential for print qualification. To accomplish this layer-wise surface topography monitoring, researchers started implementing a structured light projection methodology known as the Fringe Projection Profilometry (FPP). With a critical review of recent works on developing FPP for in-situ monitoring of powder bed fusion (PBF) processes, Dickins et al. [13] pointed out the need for advancing FPP to reconstruct higher-resolution surface across the entire powder bed area. They also presented a new FPP method by fusing multi-view point clouds from four cameras into a single high-density dataset for achieving higher accuracy and larger surface coverage. But the level of precision is lower due to the additional errors introduced by the multiple cameras and associated data fusion. In general, FPP systems typically consists of a projector and a camera, the projector projects structured light (such as sinusoidal fringe patterns) onto the target and the camera captures the reflected light patterns. The reflected light patterns are encoded with the surface topography information of the target object, which are evaluated using appropriate algorithms. FPP methods are well-known for their ability to provide high-resolution and full-field 3D map of the measured objects in a non-contact manner and within a short period of time, and thus widely used in diverse fields including human face recognition [14,15], 3D intra-oral dental profile measurements [16], and surface roughness measurement [17]. Other in-situ off-the-shelf profilometers such as Keyence profilometer are also implemented for online surface inspection in LPBF [18]. However, the field of view of the Keyence profilometer is not specified, and the limited working distance requires the profilometer to be installed inside the machine chamber close to the build plate, making it difficult to be applied to a variety of commercial LPBF printers with constrained space. Besides, those commercially available profilometers are costly and involve sophisticated operations that usually interrupt the printing process.

# 1.2. Developing fringe projection for laser powder bed fusion process monitoring

FPP offers a potential approach to realize low-cost, non-contact, high-performance in-situ surface topography monitoring of AM processes [19–22]. However, to use the FPP method for measuring the dynamic topography of the print layers during LPBF-based metal AM processes, unique challenges exist mainly because the heterogeneous material properties between and within powder and print part. For instance, distinct surface reflectivity across the powder bed tend to cause shadows and intensity saturation here and there. To mitigate the

non-homogenous reflectance issues, high dynamic range (HDR) methods [23-25] are often employed. A comprehensive review about the HDR methods for FPP is presented in Ref. [26]. In a recent work, Liu et al. report a successful implementation of an in-situ FPP system integrated with HDR methods and Support Vector Machine (SVM) based classifier for evaluating the surface morphology of parts (specifically high reflectance surfaces) printed using electron beam based metal AM [27]. While this method is promising for electron beam-based metal AM, there lacks an implementation of FPP integrated with HDR and ML for LPBF. Furthermore, the reported SVM based surface morphology evaluation is still constrained by the camera's lateral resolution. Another challenge while implementing FPP for AM is projector-camera nonlinearity (gamma correction). This is typically addressed by tuning the camera orientation angle or employing multiple cameras [28,29]. In our previous work, we solved the projector-camera nonlinearity issue by introducing a local correction factor,  $C_{xy}$  [21] which is free of additional hardware installations. Furthermore, unlike standard gamma correction which is applied as constant to all pixels, the local correction factor  $C_{xy}$  is the pixel-wise variable which considers the location effect for FPP.

On the other hand, machine learning (ML) has been increasingly applied to measure AM surface topography with the development of neural networks (NNs) for image recognition and reconstruction [30-34]. In a recent work by Shi et al. [8], authors report a use of a convolutional autoencoder (CAE) based neural network (NN) integrated with random forest classification for predicting accurate surface morphology for parts printed with various process parameters in laser engineered net shaping AM. The input for the CAE network were noisy surface profiles of the print parts evaluated using optical profilometry. However, the application of CNN and deep learning to FPP based surface topography is emerging. Recently, in Ref. [35] authors introduced a CNN based surface topography reconstruction method with an in-house developed 3D structured light scanner setup (similar to a FPP system). However, the ground truth/"test" point cloud data for the CNN was also an estimation from the developed 3D scanner setup itself and numerically simulated images (Gaussian random field) rather than more reliable measurement from an ex-situ standard equipment. This type of training data typically introduces model bias, which is not ideal for part qualification. The authors report that the developed methodology needs to be further improved from more accurate measurements of the AM parts including in-situ, online process monitoring, implementation. Researchers also implemented NNs for improving the FPP algorithms such as wrapped phase maps, and phase unwrapping calculations which then contribute to the improvement of the final target measurement result, i.e., the surface topography measurements. For instance, in Ref. [24] Zhang et al. developed a HDR based deep learning network which specifically focused on the estimation of wrapped phase with improved accuracy and reduced noise. Spoorthi et al. used a variation of SegNet framework for phase unwrapping in FPP [36,37] with improved accuracy as compared to standard phase unwrapping methods such as quality guided phase unwrapping and least squares based phase unwrapping. It must be noted that these reported NN frameworks are for general FPP algorithms, typically used for macroscale objects and were not tested on FPP for metal AM. The implementation of these NNs is promising and can aid in the improvement of surface topography measurements in metal AM.

Although implementing ML techniques to improve the FPP methodology show improved accuracy, these methods are limited to the camera lateral resolutions (sensor pixel size) and optical system's spatial frequency response (transfer function) [38]. For this reason, a novel method is needed to improve the overall resolution of FPP measurement. Image super resolution (SR) is the process of converting a given low-resolution (LR) image with coarse details to a corresponding high-resolution (HR) image with better visual quality and refined details [39]. Recently, SR has become a topic of great interest in computer vision due to both of its challenges (e.g., ill-posed inverse problem) and important applications. Deep learning approaches have ushered in

enhanced SR performance. The implementation of residual connection [40] allows to reconstruct more accurate details from LR sample through training deeper network model. Zhang et al. proposed Residual Dense Block (RDB) structures to train deep neural networks, which utilize the hierarchal features from original LR images to retrieve HR images [41]. Apart from utilizing the convolution-like structures to extract and reconstruct image features, Ho et al. proposed the de-noising diffusion probabilistic model (DDPM) [42] which is a Markov chain model trained through sampling from Gaussian noise to match the target HR in finite time. This model is further improved in Refs. [43,44] by advanced parameter schedule, the iterative de-noising mechanism, and the improved U-Net design to learn the noise added in the diffusion process. While these models show robust performance in SR tasks in the field of computer vision, there is a lack of developed SR models to advance optical metrology methods (e.g., FPP) for in-situ monitoring of AM processes (e.g., LPBF).

### 1.3. Objective of this work

The objective of this work is to enhance the discernibility, accuracy, resolution, and robustness of FPP in the specific application scenario of measuring layer-wise surface topography during LPBF AM processes by integrating our recently developed LPBF-specific FPP sensing model that features localized sensor calibration and Fourier filter-aided unwrapping with an equipment-based HDR method and machine learning (ML) aided FPP data analysis. First, a projector based HDR method is applied to mitigate the shadowing and intensity saturation problems by projecting sinusoidal fringe patterns of varying intensities. Secondly, a ML framework is developed to improve the surface topography measurement accuracy and resolution that is currently subjected to hardware limitations.

As we demonstrate the potential benefit of applying HDR based FPP (HDR-FPP) to LPBF monitoring by using a simple two-intensity projection, our work focuses on improving the end results of FPP measurement of surface topography using three potential ML models. Overall, in this work we develop a new framework of ML-aided HDR-FPP method to address the shortcomings of current LPBF surface topography measurement methods as introduced above. Specifically, a basic HDR-FPP system is implemented to acquire in situ layer-wise images of powder bed and printed layer, which are then analyzed for estimating the surface topography and height maps. Different super resolution ML models including RDB-CNN, DDPM, and DDPM-SR3 are developed to further enhance the HDR-FPP measured surface map for evaluating the layerwise surface topography maps with improved resolution in LPBF processes. The resulting surface topography is validated against ex-situ standard optical profilometry.

The remainder of this paper is divided into the following sections. Section 2 introduces the HDR-FPP methodology, experimental setup, and machine learning model specification. Then, results and both quantitative and qualitative analyses are presented in Section 3. Finally, conclusion and recommendation for future works are provided in Section 4.

### 2. Methods

### 2.1. FPP methodology

The basic principle of FPP includes the calculation of the depth or height of a target object by comparing the phase change between the original and the distorted phase maps reflected from the reference plane and the target object respectively. In FPP, typically, sinusoidal fringes are projected on to the target object surface and the projected intensity at location x and y is described in Eq. (1), where B(x,y) is the background ambient light intensity and M is the projector bias.

$$I(x,y) = B(x,y) + M(x,y)\cos(\varphi(x,y) + \delta)$$
(1)

Due to the camera-projector nonlinearity issues and their effects on the obtained results, we demonstrated an improved FPP method by applying localized intensity correction factor ( $C_{xy}$ ) in our previous work [21] as shown in Eq. (2).

$$I^{calibrated} = \frac{I^{camera}}{C_{vv}} \tag{2}$$

After the intensity correction, the wrapped phase map is calculated with three-step phase shifting algorithm as presented in Eq. (3), where N is the total number of phases (N = 3 in this study).

$$\varphi(x, y) = \arctan\left(\frac{-\sum_{i=1}^{N} I_i^{calibrated}(x, y)\sin(\delta_i)}{\sum_{i=1}^{N} I_i^{calibrated}(x, y)\cos(\delta_i)}\right)$$
(3)

The wrapped phase map is later unwrapped and compared with the reference unwrapped phase map to calculate the target height profile. The similar triangle theorem is used to derive the geometric relationship between phase value and height. Specific details in mathematical formulation and implementation procedures of the newly developed LPBF-specific FPP method can be found in our previous work [21].

### 2.2. High dynamic range method (HDR) for FPP

The intensity saturation problem cannot be completely solved using traditional gamma correction and the developed  $C_{xy}$  correction. Therefore, in this work we implement a projector based HDR method to further mitigate the intensity saturation issues. In projector based HDR method, sinusoidal fringes with same phase but different intensities are projected on the target object, and these images are fused to generate another image with average intensity features which can eliminate pixel saturation due to the high reflectance emanating from the printed part. This can be mathematically written as:

$$I_{fused}^{i} = \frac{\sum_{k=1}^{M} I_{k}^{i}}{M}, i = 1...N$$
 (4)

i represents the phase shift step and M represents the total number of various intensities images captured at phase i.

In this work we use two intensity levels, (1)  $I_1 = 250$  and (2)  $I_2 = 160$ , which can capture dark and bright parts in the specific LPBF machine setting with the specific material (Inconel 718). The numerical values of  $I_1$  and  $I_2$  correspond to the luminance or projection intensity and are chosen based on our experiment observations, which find that the average of these  $I_1$  and  $I_2$  is suitable to avoid under-/over-exposure most of the time through the entire multi-layer print across the whole print area. An illustration of image fusing with a higher and lower intensity image is shown in Fig. 1. Note that the dynamic scene of LPBF print due to heterogeneous and changing materials may necessitate the use of weighed exposures and/or adaptive projections. However, the topic of optimizing multi-image fusion weights or multiple projections requires extensive research effort and is beyond the scope of this work which is focused on exploring ML techniques to enhance HDR-FPP. Besides, only two constant projections are used in this study since taking more projections and shots or adjusting projection intensities online would require a longer period between printing consecutive layers and significantly interrupt the LPBF process. Nevertheless, the two-projection scheme can help reduce the measurement error due to LPBF process noise and camera sensor noise, and be used as a benchmark method to

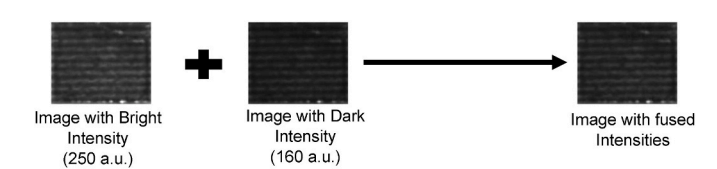


Fig. 1. Schematic of projector based HDR image fusion.

demonstrate the potential benefit of HDR compared to traditional FPP (elaborated in Section 3.1).

By substituting the intensity in Eq. (3) with the HDR fused intensities that are locally calibrated by the corresponding experimentally characterized correction factor  $C_{xy}$ , the final phase shifting formula for calculating the wrapped phase map is shown in Eq. (5).

$$\varphi(x, y) = \arctan\left(\frac{-\sum_{i=1}^{N} I_{i\_calibrated}^{fused}(x, y)\sin(\delta_i)}{\sum_{i=1}^{N} I_{i\_calibrated}^{fused}(x, y)\cos(\delta_i)}\right)$$
 (5)

After acquiring the wrapped phase map, the unwrapped phase map is calculated through 2DFFT incorporated phase unwrapping algorithm [21]. The height calculated directly from our FPP method is the print part height relative to the powder surface thus measured to be a negative value due to the powder fusion and solidification shrinkage. The surface topography in this work is defined to be the distance between the top surface of the fused part and the build plate. Specifically in a single-layer print scenario as reported in this work, the surface topography is calculated by adding the nominal layer thickness (40  $\mu m$ ) to the FPP acquired height value.

# 2.3. FPP experimental setup

The developed FPP system consists of a DLP Projector (LightCrafter 4710 EVM G2, Texas Instruments, Dallas, TX) with a resolution of 1920 × 1080 pixels, a 5 MP CMOS camera (Fastec IL5Q, Fastec, San Diego, CA), and a computer to control the two units. The FPP projector is mounted on an EOS M290 machine, and the camera is situated outside the build chamber pointed towards the build plane of the printer as shown in the Figure below (Fig. 2). Standard pin-hole camera calibration is applied to retrieve the intrinsic parameters of the camera along with the rotation and translation matrices for perspective correction, and details of pin-hole camera model formulation is presented in the Supplemental Information (SI) Section 1 [45]. The printer has a build chamber of 250  $\times$  250  $\times$  325 mm<sup>3</sup> and is equipped with a single mode 400 W continuous wave ytterbium fiber laser. Compared to the setup shown in our previous work [21], the experiment setup presented in this work adopts the monochrome camera for image acquisition. The camera choice shifts from colored to monochrome as the monochrome sensor has high details and sensitivity as opposed to color sensor. Limited by its color filter array (CFA) design, color sensor captures less details and more sensitive to intensity saturation [46].

## 2.4. Experimental test cases

A total of 39 single-layer square blocks (10 mm  $\times$  10 mm) were printed on a 4  $\times$  4-inch build plate (Fig. 3). The layer height for these



Fig. 2. The physical setup of our FPP system.



Fig. 3. LPBF printed single-layer blocks in our experiment.

scans is set to be 40 µm. As shown in Fig. 3, due to a placement error the right column of printed samples is print slightly outside the build plate. The out-of-region prints are not considered for data analysis. Ex-situ measurements on this build are performed using an optical 3D profilometer (Keyence VR3200, Keyence Corporation of America, IL, USA). The HDR-FPP method outputs the surface topography with lateral resolution of ~38 um while the ex-situ characterized HR profilometry surface topography has the lateral resolution of  $\sim$ 5  $\mu m$ . The details of the empirical calibration results including both localized  $K_{xy}$  and  $C_{xy}$  are presented in the SI Section 2 - Figs. S1 and S2. The unwrapped phase map extracted from the raw image data are further filter by the masked (or spatially selective) 2D FFT filter to reduce the sinusoidal artifacts caused by phase jump which is elucidated in the SI Section 3 – Fig. S3. The FPP and ex-situ profilometry data from this build are used to train the machine learning models for the estimation and generation of highresolution height maps presented in Section 3.

# $2.5. \ \ \textit{Deep learning-based surface topography super resolution}$

# 2.5.1. Data preparation for ML models

The surface topography measurement data can take on a variety of forms such as 3D point cloud and 2D image. Researchers commonly employ a point cloud to describe a surface topography and align or compare point clouds of spatial data measured by two equipment (e.g., FPP and microscope) using iterative closest point method. However, unlike images, point clouds don't have a rigid structure, posing challenges in deep learning for point clouds which involve huge computational complexity. It is still difficult to develop effective and efficient neural networks for large-scale point clouds, while image-based ML models have been well developed and widely used. Therefore, in this work we adopt the image form to represent surface topography data from the in-situ FPP and ex-situ microscope. Specifically, grayscale images are generated by converting the measured height values into grayscales with a linear transformation between a custom-defined constant height range [-30  $\mu m$ , 50  $\mu m$ ] and an 8-bit grayscale range [0, 255]. It is worth pointing out that the conversion between the height values and integer grayscales will not give rise to a significant loss of resolution and precision in the case of LPBF layer thickness measurement. To illustrate, in this work, one grayscale level corresponds to [50

 $\mu m - (-30~\mu m)]/255 \approx 0.314~\mu m$ , which is acceptable and definitely can be improved by using a 12-bit or even 16-bit grayscale images. Moreover, please note that the height range is chosen based on the LPBF process parameter – layer thickness (40  $\mu m$  in this study) and can cover all possible height values during LPBF printing of each layer. The specified height range also determines the input and output height range of the upcoming ML models, i.e., the surface height range of the ML models' predictions. Users of our approach developed in this work can select the height range based on their specific LPBF process setting to generate grayscale images of surface topography, which can be used to train their own ML models using the same methods and algorithms as presented in subsequent sections for predicting surface topographies in their LPBF monitoring applications.

After obtaining the LPBF printed samples' grayscale images that encode the corresponding height maps measured by in-situ FPP and exsitu microscope, we directly align the in-situ and ex-situ measurement images by aligning to the same single edge line and assuming that the inprocess part (measured by in-situ) is uniformly scaled to the post-print part (measured by ex-situ) across the entire surface area. We further divide the in-situ and ex-situ grayscale images into a grid with the same number of rows and the same number of columns. Thus, we consider that each sub-region (i.e., each grid area) in the in-situ image corresponds to a sub-region at the same grid location (same index of grid column and row) in the ex-situ image. Like any other registration methods, this method using a single edge to align the two images is also subjected to alignment errors due to the different resolutions and human eye error, which is estimated to be  $\pm 40~\mu m$  error in total in case of being misaligned by one line (i.e., one pixel in FPP camera). This alignment error can be reduced by improving the optics design or using higherresolution camera with smaller pixel size in FPP. Another issue lies in the assumption of spatially uniform scaling between the in-situ and exsitu parts. This assumption might not hold for many reasons including the LPBF process variation such as stochastic laser fluctuation and heterogenous material properties as well as nonuniform post-build cooling and shrinkage effects. However, it is such a realistic mismatch between in-situ and ex-situ parts that motivates this work to exploit ML for capturing these hidden or inaccessible cause-and-effect relationships and predicting the post-build part surface with better accuracy and prediction by only using in-situ monitored process signatures (e.g., FPP) without the need for extensive ex-situ characterization.

Overall, to transform the FPP acquired surface topography into inputs for SR models, some preprocessing steps are required. In this work, the FPP measured surface topography of a printed  $10~\text{mm}\times~10~\text{mm}$  sample block is transformed into a 256 pixels  $\times$  256 pixels grayscale image with a lateral resolution of  $\sim\!38~\mu\text{m}$ , and the ex-situ profilometer measured surface topography transforms into 2048 pixels  $\times$  2048 pixels grayscale image with a lateral resolution of  $\sim\!5~\mu\text{m}$ . As shown in Fig. 4,

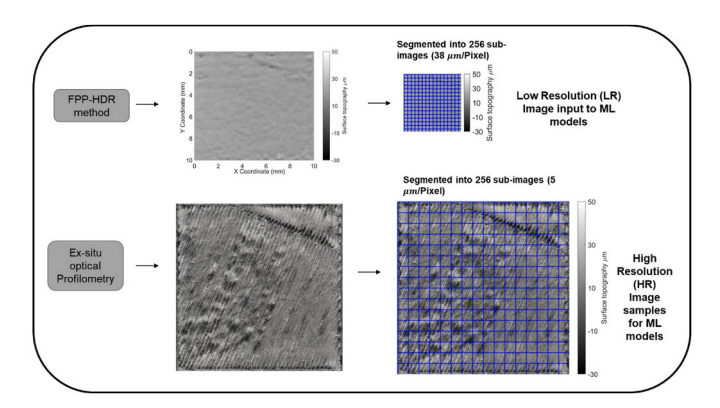


**Fig. 4.** Schematic of the surface measurement data preprocessing (Yellow block from Fig. 3 used as the example). (For interpretation of the references to color in this figure legend, the reader is referred to the Web version of this article.)

the surface topography measurements from in-situ FPP and ex-situ optical profilometer are further segmented into 256 sub-images to create a sufficient dataset for ML training and testing. After image segmentation, the next task is to map LR to HR using the proposed ML models described in the following sections. As shown in Fig. 4, after the data preprocessing, the objective of the work is to find the latent representation from the low resolution in-situ FPP monitored surface topography which is embedded in to 16 pixels  $\times$  16 pixels grayscale images, and then use the latent representation to reconstruct the high resolution (256 pixels  $\times$  256 pixels) grayscale images acquired from ex-situ profilometer.

A total of 8192 paired LR and HR sub-images are segmented from 32 printed single-layer blocks (Fig. 3). In this work, to avoid the potential data leakage problem in machine learning model training, three datasets are prepared by randomly selecting 70% of the segmented images within each individual block as training set, 10% images within each individual block as validation set, and the rest 20% images as testing set. The reason we don't use whole blocks as training, validation, or testing samples is that each block sample tends to exhibit some different features due to the build location effect and different laser scan strategies. For example, while printing the 32 blocks, although the scan angle is set as 67° for all of them, the specific laser stripe overlapping locations and each scan's start and end locations are different, leading to different surface topography as seen in Fig. 3. Therefore, the current dataset split strategy using segments of each block will allow the models to learn various possible features from the samples that are printed at different locations across the build plate under different processing conditions.

#### 2.5.2. RDB-CNN model

Deep convolutional neural network is implemented in this work as a super resolution model to correlate the in-situ FPP calculated surface topography and the ex-situ characterized HR surface topography. We propose to implement CNN with both dense and residual connections [41,47] which takes the encoded FPP result in gray-scale as input and optical microscopy measured surface topology encoded in gray-scale as output. The major advantage of using residual and dense structure-based (RDB) CNN is that it performs the feature extraction directly from LR images' hierarchal features, and the upscale step happens after all the required feature extraction and fusion is complete. Furthermore, the RDB utilizes both residual and dense connections which allow features to flow from blocks to blocks. As shown in Fig. 5, the LR image is first processed by two convolutional layers with kernel size of 3, padding 1, and stride 1 to extract features into 64 channels. After the two convolution operations, the extracted feature map is further processed by a series of individual RDB. Each RDB is composed of stacked convolution layers with dense connections (Fig. 5). All the layer activation functions are ReLU. The upscaling layer is implemented based on Efficient Sub-Pixel Convolutional Neural network (ESPCN) [48] followed by convolution layer to output desired HR image size. The specific details related to residual connection and dense connection are included in Appendix Section (A).

 $L_1$  loss function is used for calculating loss between target output and the predicted HR output. The implemented  $L_1$  loss function is shown in

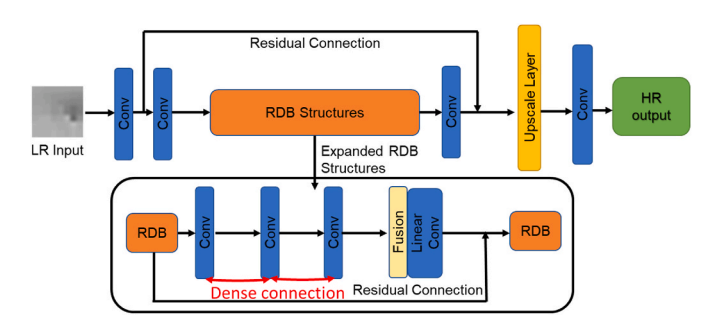


Fig. 5. RDN structure for image super resolution.

Eq. (6).

$$L_{l} = \sum_{i=1}^{N} \left| y_{true} - y_{predicted} \right| \tag{6}$$

The RDB-CNN model implemented uses the Adam optimization method [49]. The output from the model is a one channel HR grayscale image.

As mentioned earlier,  $3\times 3$  kernal filter is implemented to all the convolution layers except for the fusion layer (annotated in Fig. 5) which  $1\times 1$  convolution is used. Three RDBs are implemented inside the RDB structures while each RDB is constructed with three densely connected  $3\times 3$  convolutional layers for feature extraction, and more details can be found in Appendix 1. To preserve the sizes of all tensors, zero padding are automatically enabled. In this specific task of super resolution, no regularization term is enforced to the loss function and neural network as all the features reconstructed are from training dataset. The model is optimized through backpropagation using Adam [49].

### 2.5.3. Denoising diffusion probabilistic model (DDPM)

The second image super resolution model utilized is DDPM models which is a model trained based on Bayesian inference and Markov process. The diffusion probabilistic model (DPM) first diffuses a target image through adding standard Gaussian noise and constructs a parametric model to learn the diffusion process. A transitional Markov process is learned by the model through ML for reversing the diffusion to match the target images. The specific model derivation and hyper parameters assumption are included in Appendix Section (B). DDPM models first diffuse the target HR image at training stage (denoted in probabilistic distribution q in Figure A-2) and learns the noise added at any given time step during the diffusion process. Then the model performs the reverse process at inference stage (denoted in probabilistic distribution p in Figure A-2).

$$L = |f(x, \alpha_t, \widetilde{y}, \beta_t) - \varepsilon|_1^2$$
(7)

The loss function for the proposed neural network is shown in Eq. (7) where  $f(x,\alpha_t,\widetilde{y},\beta_t)$  is the objective function composed of input LR image x, the diffused image  $\widetilde{y}$  at the given time step, and hyperparameters.  $\epsilon$  is sampled from standard Gaussian distribution through training steps as the manually added noise. Comparing to other CNN based ML model like RDN which learns the direct mapping between LR and HR from previous section, DDPM learns the latent variable (statistical noises) through UNet structures to reconstruct HR details.

After training the designed neural networks, the inference process is proceeded by subtracting the noise from the image, denoted as reverse process *p* in Figure A-2. In this work, two variants of DDPM models are applied to acquire HR surface topography: standard DDPM and DDPM-SR3. The difference between the two models is that DDPM-SR3 implements iterative refinement steps in inference step of the model. The training results are presented in subsequent sections to compare their performance specifically in reconstructing HR layer-wise surface topography for additive manufactured part.

### 3. Results

### 3.1. HDR FPP results and comparison

Following the experiment setup and the HDR-FPP methodology (Section 2.3), height maps for all 39 single layer print blocks are calculated. To elucidate the effectiveness of implementing HDR method to mitigate the noise and errors caused by high intensity saturation, the block enclosed in red rectangle shown in Fig. 3 is selected and its surface topography is obtained using our proposed HDR-FPP method and the FPP method that we recently improved by introducing  $C_{xy}$  and 2DFFT [21] which still cannot address the shadowing and over-exposure issues due to using a single projection intensity (250 a. u.).

As shown in Fig. 6, the HDR-FPP calculated surface topography displays less noise compared to the surface topography acquired by the recently developed FPP [21]. The previous FPP method introduces more intensity saturation errors that can be discerned visually along the left bottom stripe. While the qualitative comparison reveals that implementing the HDR-FPP method mitigates the pixel saturation issue, a quantitative analysis is also conducted between existing FPP, new HDR-FPP, and ex-situ optical profilometer (HR) by extracting the line profile 2 mm from the left edge of the block.

As shown in Fig. 7, the extracted line profiles exhibit similar surface topography trend. Some mismatches exist because the ambient light condition and gas flow inside the LPBF machine could affect the in-situ measurements but not the ex-situ characterization. Another primary reason is that the FPP and HDR-FPP methods both have lower lateral resolution than the ex-situ profilometer. This issue will be addressed in the subsequent section. Due to the resolution difference between in-situ FPP and ex-situ profilometer, the quantitative comparison is performed by downscaling the ex-situ profilometer measured data through average filtering. The root mean squared error (RMSE) between the FPP and exsitu profilometer is  $10.57 \mu m$ , and the RMSE between the HDR-FPP and ex-situ profilometer is 8.9 µm. Quantitatively, the HDR-FPP measures the layer-wise surface topography more accurately compared to the existing FPP method. The implementation of projector based HDR method improves the performance of FPP method and ensures the applicability for real-time measurement by only projecting two different levels of intensity. The experimental result from the block printing experiment also reveals that the projector based HDR method mitigates the phase error which is primarily dependent on ambient light condition, fringe density, and sensor noise from camera. The block (enclosed in blue from Fig. 3) acquired FPP images are subjected to high camera sensor noise due to loss of focus in certain regions, and its surface topography shown in Fig. 8 reflects the observable phase errors and fluctuation which induce the error in height calculation comparing to the ex-situ profilometer measured surface topography. Visually, the abnormal fast spatially height variations indicate the high phase error which is reduced using HDR method.

# 3.2. Machine learning super resolution model results

The results shown above indicate a need for improving the HDR-FPP accuracy further to match the ex-situ standard profilometer measurement. In this section we demonstrate a ML enhanced HDR-FPP method with three ML models - RDN, DDPM, and DDPM-SR3, in order to improve the acquired HDR-FPP surface topography resolution from ~38  $\mu m$  to  $\sim 5~\mu m$ , thus enhancing the HDR-FPP measurement performance. As elucidated in Section 2.5.1, the 32 sample blocks' (Fig. 3) surface topographies encoded grayscale images are segmented into 8192 sub images (patches) to create a dataset for training, validation, and testing. The specific super resolution task is to predict HR profilometer measurement (128 pixels × 128 pixels) from input LR FPP measurement (16 pixels  $\times$  16 pixels). All the three types of ML models are trained with supervision to ensure local convergence. For each of the models trained, the specific iterations with lowest validation loss are used as the trained model for predicting the surface topography of the completely unseen sub-images (i.e., segments) in the test set. The training loss and validation accuracy of the final best model is shown in the Appendix Figure A-

Several sub-image samples from sample block (enclosed in yellow from Fig. 3) are chosen and the results are presented in Table 1.

The results as presented in Table 1 indicate that DDPM-based models' predictions visually agree with the target HR image (ground truth), while the RDN model, a feature extraction-based CNN model, could not reconstruct most of the important details. Further, to quantify the prediction accuracy, two common metrics, Peak Signal-to-Noise Ratio (PSNR) and Mean Squared Error (MSE), are selected to quantitively evaluate the models. PSNR calculates the ratio of the maximum

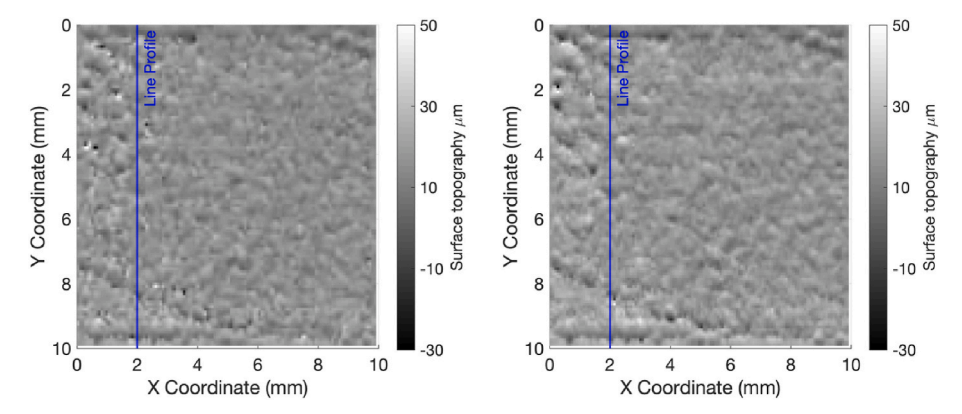


Fig. 6. Our previous FPP method (left) vs current HDR-FPP method (right): surface topography of the red block from Fig. 3. (For interpretation of the references to color in this figure legend, the reader is referred to the Web version of this article.)

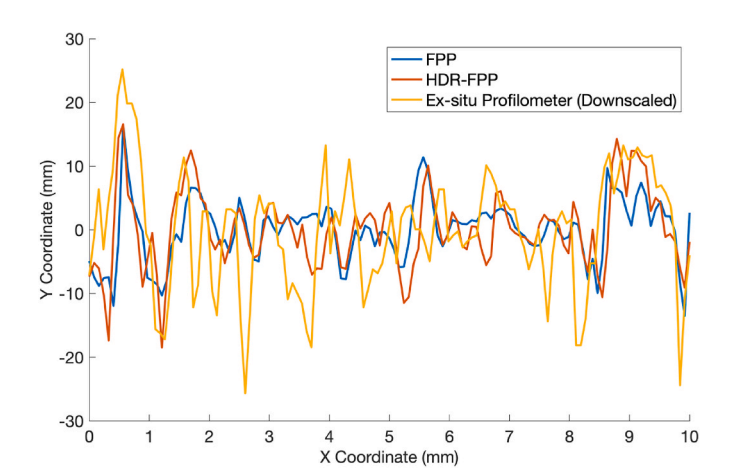


Fig. 7. Extracted line profile from Fig. 6 comparison between FPP, HDR-FPP, and ex-situ profilometer.

possible grayscale pixel value from LR input image and the MSE. Further, it can manifest the performance of model in capturing major local features from the image by focusing on features from maximum possible grayscale pixel value. The MSE error indicates the average deviation between predicted results and target HR images and can provide an estimate of global measurement accuracy accounting for each pixel's measurement deviation. Besides, PSNR is an illuminance-based metric which provides an indication of better visual quality, i.e., higher PSNR means the prediction incorporates the primary features of target HR image. The PSNR is computed using Eq. (8) where  $\text{Max}_{\text{g}}$  is the maximum possible grayscale pixel value and MSE is the mean squared

error between predicted HR image and target HR image measured through ex-situ characterization. In this case, the MSE metric has the units of grayscale  $\rm value^2$ .

$$PSNR = 10 \log_{10} \left( \frac{Max_g^2}{MSE} \right)$$
 (8)

As shown in Table 2, the arrow indicates the desired trend of the metric. Based on the quantitative measurement, DDPM-SR3 outperforms RDN and DDPM in both scales which proves its validity in reconstructing HR details in the LPBF printed part scenario. Although MSE metrics tend to penalize the generated HR details according to Eq. (15), the DDPM-SR3 model can predict most local features (reflected by the highest PSNR in Table 1) with best global accuracy (reflected by the lowest MSE in Table 1), making it advantageous in contrast to the other two models. Compared to DDPM-SR3, standard DDPM model has a relatively lower decent performance by the metrics of PSNR but far outperform the RDN method especially in terms of MSE. It should be noted that RDN performs poorly in this specific super resolution task due to the different mechanisms of RDN model and DDPM like model. While DDPM like model is a synthetic/generative model which generates and samples the details based on the training dataset, RDN purely relies on the LR images which has no hidden revelation and clues of detailed features that need to be reconstructed. In this case, the lower resolution surface topography acquired from FPP has less information in surface textures comparing to the direct down-scaled high resolution ex-situ measured surface topography through average filter.

The work above evaluates our proposed ML models on sub images that are segments of the target measurand in test dataset. The ultimate goal of the designed ML frameworks is to predict the surface topography of a whole block printed by LPBF. To this end, the predicted sub images

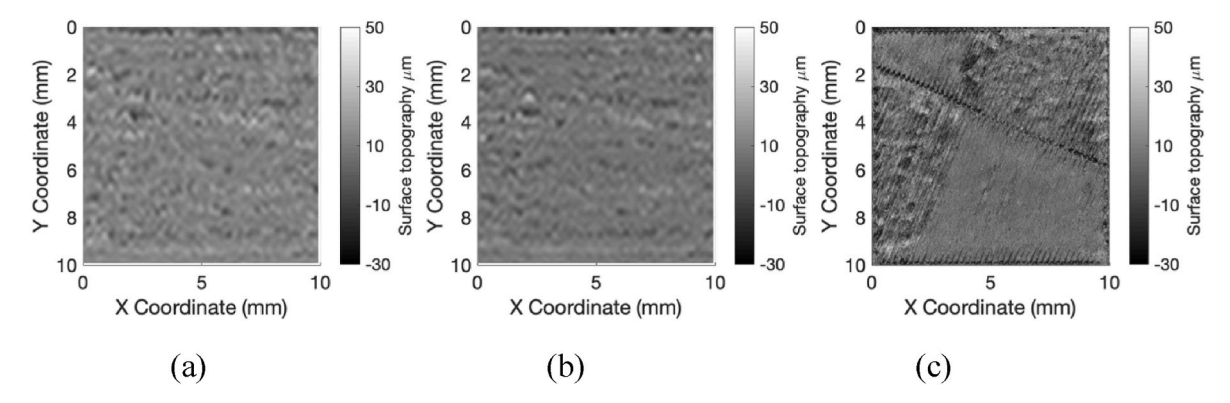


Fig. 8. (a) Surface topographies (blue block from Fig. 3): (a) FPP; (b) HDR-FPP; (c) Ex-situ profilometer measurement. (For interpretation of the references to color in this figure legend, the reader is referred to the Web version of this article.)

**Table 1**Predicting a test set sample's surface topography from trained Super Resolution models (The original HDR-FPP measurement result is shown in the left column to show the effect of ML enhancement on HDR-FPP accuracy).

EDD LIDD DDM DDM DDDM CD2 LID Toward (Committee of the Committee of the Co							
FPP-HDR	RDN	DDPM	DDPM-SR3	HR Target (Ground			
(16 X 16	(128 X 128	(128 X 128	(128 X 128	Truth)			
pixels)	pixels)	pixels)	pixels)	(128 X 128 pixels)			
*							
=							
=							
-							
-							

 $\begin{tabular}{ll} \textbf{Table 2} \\ PSNR \& MSE on sub-images of 16X16 to 128X128 HDR-FPP measured surface topography super resolution. \end{tabular}$ 

	RDN	DDPM	DDPM-SR3
PSNR (dB) ↑	11.23	18.56	22.07
MSE (grayscale <sup>2</sup> .) ↓	6756	1058	767
MSE $(\mu m^2) \downarrow$	665	104	75

from different models are merged and compared with the HR surface topography encoded image obtained from the ex-situ standard profilometer. To further decode the predicted grayscale image into surface topography map with units of micron, the colormap transformation is adopted to transform the grayscale value from 0 to 255 to  $-30 \mu m - 50$  $\mu$ m. For this reason, one grayscale value corresponds to 0.313  $\mu$ m. It should be noted that the ex-situ microscopy implemented in this work has the vertical resolution of 1  $\mu$ m, larger than one grayscale represented height (0.313  $\mu$ m). This means that encoding the FPP measured height into a grayscale ranging between 0 and 255 will not affect the best achievable vertical resolution determined by the labeling data resolution (i.e., ex-situ microscopy) used in machine learning. It also indicates that the machine learning aided HDR-FPP method can enhance the vertical resolution from 10  $\mu m$  (original HDR-FPP measurement) to 1  $\mu m$ (as reported in this work). The decoded surface topography (from grayscale to height value) from the prediction result of DDPM-SR3

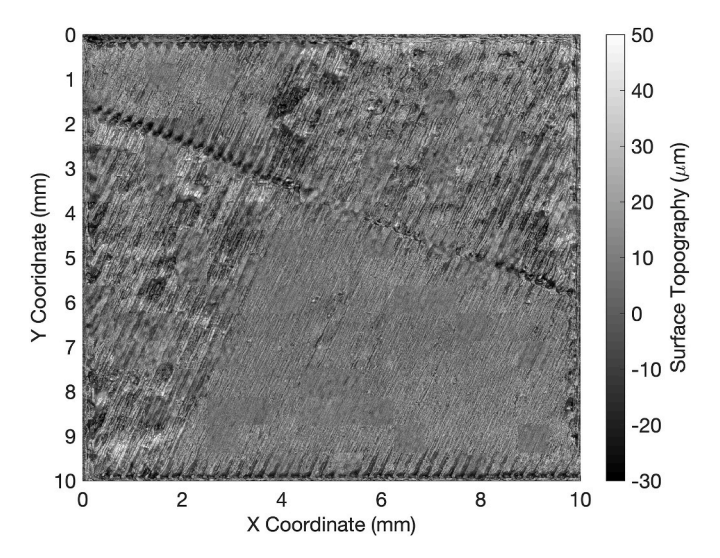


**Fig. 9.** Decoded surface topography of the same block as shown in Fig. 8 from ML (specifically, DDPM-SR3) model prediction using HDR-FPP measurement data as input.

model is shown in Fig. 9, which shows a much better agreement with the ground truth compared to these non-ML-aided FPP results as shown in Fig. 8.

Fig. 10 shows our test result of a representative block's surface topography (enclosed in red from Fig. 3) from different models. It reveals that the DDPM-SR3 outperforms all the other proposed models in terms of the predicted surface topography's visual quality. Using the same quantitative metrics described above, the comparison for merged surface topography encoded image is shown in Table 3. For the merged complete surface topography, the DDPM-SR3 and DDPM models do not exhibit as good performance as shown for the sub image results (Table 1). This is because the developed sub-models cannot connect the details between the sequence of sub-images. To fully exploit the potential of the developed DDPM-based model for enhancing HDR-FPP, in the future, some memory mechanism or attention mechanism (e.g., gates operation from (Long short-term memory) LSTM, patch selfattention from vision transformer) will be developed to store and pass information between data sequence. Furthermore, it should be noted that the super resolution models trained in this study are essentially based on interpolation and sampling, and the reconstructed features are learnt from the training dataset. This special characteristic makes the trained models prone to generalization errors especially in this case where the upscaling factor is 8 times. Mode collapse could also be induced for samples with similar LR features (smooth texture from FPP measurements). In the future, more validations work is needed to validate the transferability of these models.

Based on the above analysis, DDPM-SR3 shows dominant advantages under two common metrics (PSNR & MSE) over all other proposed

**Table 3**PSNR & MSE analysis for performance of developed models to predict the merged complete surface topography (The original HDR-FPP measurement performance is shown on the left column for comparison).

	HDR-FPP	RDN	DDPM	DDPM-SR3
	(LR)	(HR)	(HR)	(HR)
PSNR (dB) ↑	n/a	13.26	18.92	22.27
MSE (grayscale)	589	3068	834	386
MSE (μm <sup>2</sup> ) ↓	58.02	302.00	82.11	37.94
RMSE ( $\mu$ m) $\downarrow$	7.6	17.4	9.1	6.2

models, and the predicted HR surface topography is also consistent with the target images. It proves the capability of DDPM-SR3 enhanced HDR-FPP in reconstructing HR details of surface topography that is not directly available from the original HDR-FPP measurement data. Shown in Fig. 11, the same line profile from Fig. 7 is extracted from MLenhanced HDR-FPP model with DDPM-SR3 and compared with ex-situ profilometer measured and HDR-FPP line profiles. It can be observed that the ML enhanced model not only predicts the line profile with more points (high resolution), but also achieves better accuracy. Quantitatively, the RMSE between the ML-enhanced HDR-FPP model and the exsitu profilometer measurement is 7.49  $\mu$ m which is slightly better than the 8.90  $\mu m$  in the HDR-FPP and much better than the 10.57  $\mu m$  in existing FPP. It should be noted that the ML-enhanced HDR-FPP provides higher resolution which translates to more points spatially, and the ML-enhanced HDR-FPP model can retrieve surface details at 5 μm scale, much smaller than the resolution (38  $\mu$ m) in both the existing FPP and

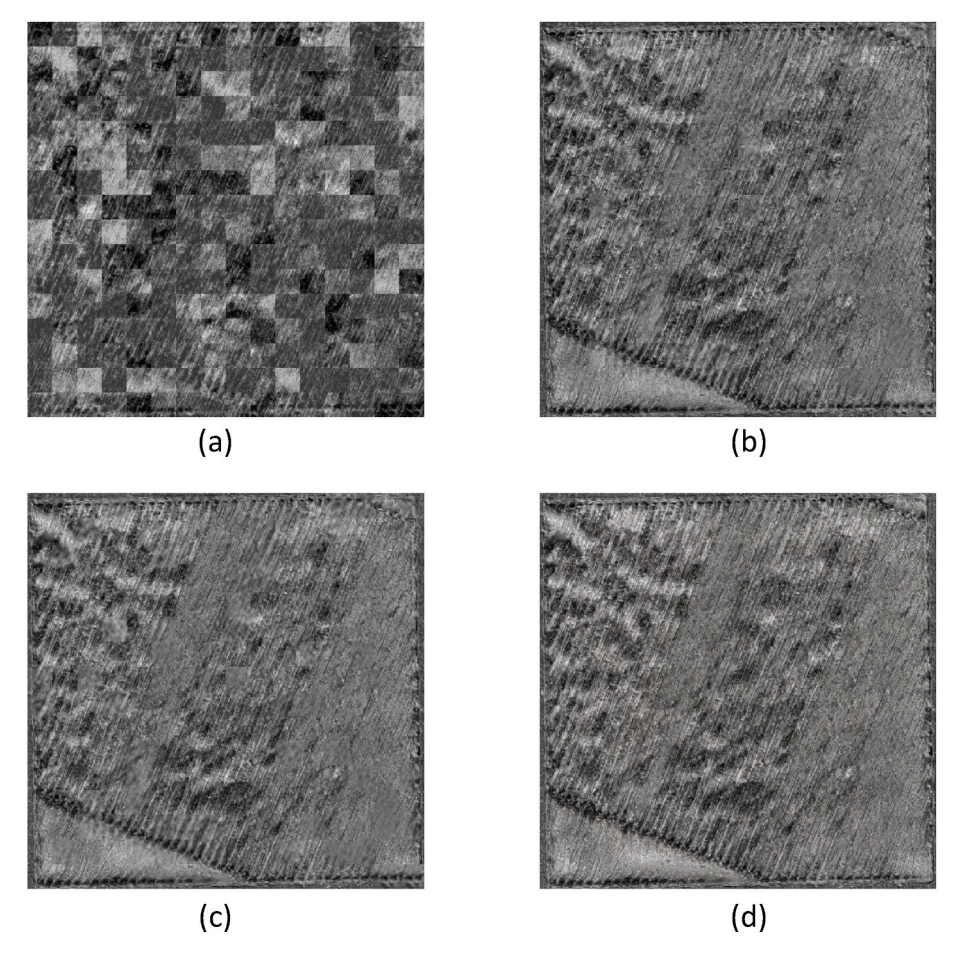
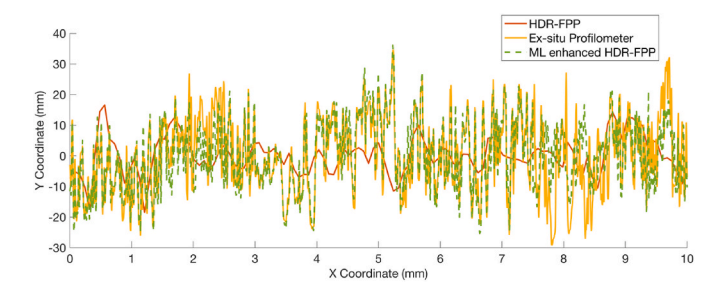


Fig. 10. Representative result of a merged block's surface topography encoded in grayscale for the printed block (enclosed in red as shown in Fig. 3): (a) RDN, (b) DDPM, (c) DDPM-SR3, (d) Ex-situ profilometer measurement. (For interpretation of the references to color in this figure legend, the reader is referred to the Web version of this article.)



**Fig. 11.** Same line profile comparison as Fig. 7, between HDR-FPP, ML enhanced HDR-FPP, and ex-situ profilometer measured surface topography.

new HDR-FPP. For this reason, the overall RMSE metric for the entire line profile here may not be treated as the essential comparison as it is biased when comparing low resolution data to high resolution data. For this reason, a less biased comparison is conducted by dividing the ML enhanced HDR-FPP line profile into 1) counterpart points that are exactly corresponding to the points existing in the HDR-FPP measured line profile; and 2) reconstructed points that are inferred by machine learning. Results reflect that when comparing the counterpart points of the ML enhanced HDR-FPP line profile to the original HDR-FPP, the RMSE is reduced from 7.49  $\mu m$  (Section 3.1) to 4.35  $\mu m$ , while the new points inferred by the ML models has a RMSE of  $9.72\,\mu m$ . By these RMSE values, we find that the ML enhanced HDR-FPP method not only can further improves the accuracy of existing HDR-FPP measurement results (lower resolution points) but also can estimate with decent accuracy the surface topography at points that cannot directly resolved by original FPP or HDR-FPP due to the hardware and optical system's constraints.

Moreover, the single line comparison here does not reveal the performance of the model for the whole block or sub-region. As shown in Table 3, the ML-enhanced HDR-FPP model outperforms the HDR-FPP under both metrics considering the whole block scenario. The PSNR is calculated for each sub-image sample to gain more comprehensive understanding about the generalizability and generalization errors from the model. As presented in Fig. 12, the mean PSNR of the DDPM-SR3 model on test dataset of 1638 sub-images is 20.77 with the standard deviation of 3.24. The distribution has the positive skew toward high PSNR value, exhibiting the robustness of the model on unseen dataset for the super resolution task of enhancing FPP measurement.

It should be noted that while the HDR-FPP performs better than

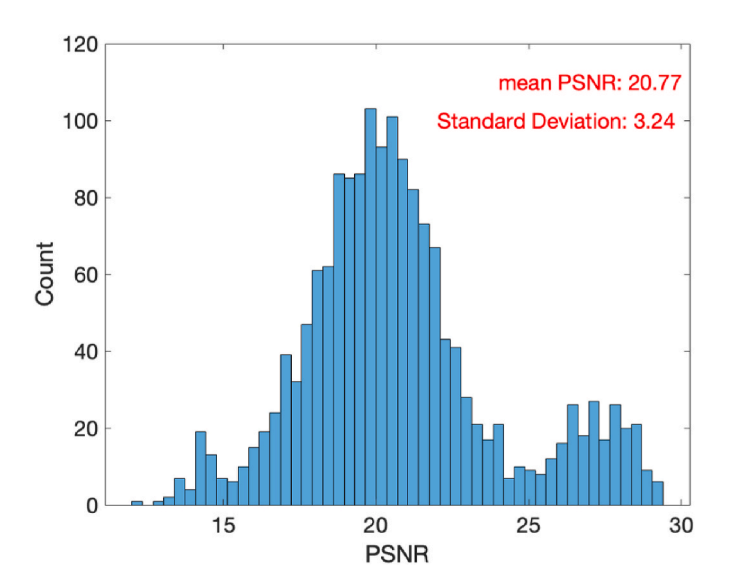


**Fig. 12.** The distribution of the PSNR of DDPM-SR3 on tested dataset of 1638 sub-images which are completely unseen during the model training and validation.

machine learning method such as RDN enhanced and DDPM enhanced models, the resolution is significant lower in HDR-FPP stance. The MSE for HDR-FPP is calculated using the down sampled surface topography from ex-situ profilometer measurement. Furthermore, while RDN performs poorly, it is more computational efficient compared to the DDPM-like models. One significant issue of the DDPM model is the slow sampling rate at each inference step during reverse-diffusion process. In this specific application scenario of surface topography super resolution, the inference time of DDPM models on a Nvidia V100 32 GB GPU node is around 10 min. For in-situ application, it requires considerable computational resources. Some implicit diffusion models which can reduce the computational complexity need to be investigated and implemented in the future for cost-effective in-situ monitoring applications.

The DDPM models trained in this work show the applicability in surface topography simulation and generation. By using the developed model, one can predict/reconstruct the  $\sim 5 \, \mu m$  lateral resolution surface topography from the LR FPP acquired surface topography with resolution  $\sim 38 \, \mu \text{m}$ . This advancement makes the detection of small powder spatter redeposition and porosity possible. Furthermore, the trained synthetic/generative models - DDPM and DDPM-SR3 can reproduce near-realistic surface topography samples for LPBF manufacturing process from pure Gaussian Noise. Since ML models or data-driven models usually require large training datasets and it is always expensive to conduct empirical study for metal AM studies, generative models such as the DDPM models trained in this work show their applicability in surface topography simulation and generation in AM processes. Another potential method is to use GAN (generative adversarial neural network) [50]. These ML methods open up an avenue to generate synthetic images which are representative of the manufacturing processes with adequate details for ML model training to enable more accurate and reliable AM processes monitoring and qualification.

### 4. Conclusion

In this work, a new ML enhanced HDR based FPP method is developed to improve the performance and measurement capability of existing FPP methods. First, a projector based HDR method is demonstrated to successfully mitigate the shadowing and pixel intensity saturation problems and improve the overall measurement accuracy by comparing to the ex-situ high-resolution profilometer characterization result. The MSE between the HDR-FPP method and the ground truth of ex-situ profilometer result is 8.90 µm and the ML enhanced HDR-FPP method achieves a MSE of 4.35 µm for a representative line profile under the same resolution. Moreover, the developed ML enhanced HDR-FPP model is capable of reconstructing high-resolution details that is not available from the original HDR-FPP acquired surface topography with an appreciable RMSE error of 9.72 µm. The proposed HDR method also reduces the phase error primarily caused by the camera sensor noise and ambient light condition. It should be noted that our subsequent work of ML enhanced HDR-FPP takes the HDR-FPP measurement model output as an input to a machine learning model for increasing both the lateral and vertical resolutions which are strictly limited by hardware setup (camera) for standard FPP methodology.

Specifically, three ML models are developed to further improve the measurement capability of the HDR-FPP method through resolution enhancement. Our results show that while traditional convolution feature extraction-based model (RDN) performs poorly on this specific task, the new image synthetic/generative models (DDPM, DDPM-SR3) yield significant improvement. The predictions from these DDPM-based models show agreeable visual quality. Further quantitative analysis by using PSNR and MSE metrics also indicate that DDPM-SR3 outperforms RDN and DDPM. The DDPM-SR3 model can predict high-resolution details from low-resolution FPP acquired surface topography. It is worth noting that the details predicted through DDPM models are not subjected to FPP hardware achievable resolution. Being a

synthetic model, DDPM is also capable of generating realistic surface topography from Gaussian noise which solves the problem of inadequate dataset in case that repeated experiments are expensive and time consuming.

To conclude, the developed ML (DDPM-SR3) enhanced HDR-FPP framework can effectively mitigate the shadowing and intensity saturation issues in current FPP methods as well as enhance the measurement accuracy and resolution. Specifically, the improved accuracy is reflected by our results as listed below.

- 1) The RMSE value for a sample line profile is reduced from 10.57  $\mu m$  (existing FPP method) to 8.90  $\mu m$  (our DDPM-SR3 enhanced HDR-FPP method) for an entire line including the reconstructed points and 4.35  $\mu m$  for the FPP directly measured points.
- 2) The RMSE value for a reconstructed or predicted segment of the same sample line profile, which cannot be directly measured by existing FPP or the HDR-FPP, reaches a RMSE of 9.72  $\mu$ m. This is better than existing FPP (10.57  $\mu$ m) and comparable to our HDR-FPP (8.90  $\mu$ m).
- 3) The MSE value for an entire block sample is reduced from  $58.02 \, \mu m^2$  to  $37.94 \, \mu m^2$ , and the corresponding RMSE value for measuring the block is reduced from  $7.6 \, \mu m$  to  $6.2 \, \mu m$ .

Meanwhile, the enhanced resolution is reflected by the following outcome from our method, i.e., ML (DDPM-SR3) enhanced HDR-FPP.

- Better resolved details and features that are not visually observable in conventional FPP results.
- 2) Lateral resolution enhanced from  ${\sim}38~\mu m$  to  ${\sim}5~\mu m$ .
- 3) Vertical resolution enhanced from ~10 µm to 1 µm (promoted by machine learning of the high-resolution ex-situ microscope measurement data).

The work also shows the potential of applying novel super resolution computer vision models, especially generative models, to monitor LPBF process and other AM processes. In the future, more sophisticated HDR-FPP methods can be explored such as hybrid-quality-guided phase fusion model [51]. To improve the ML performance while merging large

surface topography maps, some attention or memory mechanism will be incorporated to capture the relation patterns between sub images. Such ML enhanced HDR-FPP can measure the surface topography of printed layers during LPBF-AM more capably and efficiently. Thereafter, comprehensive analysis of the measured surface topography will be used to detect and extract layer-wise defects such as small bump, powder spatter, and hole, thus advancing the existing state-of-the-art methods towards the desired online inspection of LPBF print defects.

### Declaration of competing interest

The authors declare the following financial interests/personal relationships which may be considered as potential competing interests: Xiayun Zhao reports financial support partially provided by the US Department of Energy (Award Number: FE0031774) and the National Science Foundation (NSF Award Number: 2052662) industry/university cooperative research center (IUCRC) sponsored Center for Materials Data Science for Reliability and Degradation (MDS-Rely). Xiayun Zhao reports a relationship with University of Pittsburgh that includes employment.

### Acknowledgements

Authors acknowledge the financial support partially provided by the US Department of Energy (Award Number: FE0031774) as well as the National Science Foundation (NSF) sponsored Center for Materials Data Science for Reliability and Degradation (MDS-Rely) - a joint industry/university cooperative research center (IUCRC) (NSF Award Number: 2052662). Any opinions, findings, and conclusions or recommendations expressed in this publication are those of the authors and do not necessarily reflect the views of the NSF. This work used the NSF sponsored Advanced Cyberinfrastructure Coordination Ecosystem: Services & Support (ACCESS) resource - Pittsburgh Supercomputing Center Bridges-2 GPU and Storage through allocation MCH210015. Authors would also like to thank the facilities support from ANSYS Additive Manufacturing Research Laboratory (AMRL) at the University of Pittsburgh and Brandon Blasko for his help with experiment.

## Appendix A. Supplementary data

Supplementary data to this article can be found online at https://doi.org/10.1016/j.precisioneng.2023.06.015.

## Appendix

### (A) Residual and Dense layer connection

As proposed in Ref. [40], the residual connection between convolution layers eases the gradient vanishing problem, allowing the development of deeper neural networks model. Specifically, the residual connection is shown in Figure A1(a). The residual connection outputs the summation between F(X) and X as the input to next set of layer blocks while the dense blocks concatenate all the previous blocks' feature maps together (Figure A1(b)). Supposing the first convolution layer takes the 16\*16\*64 tensor as the input (kernel size of 3, padding 1, stride 1), the third convolutional layer takes both the feature map output from first and second convolution layers, forming the input feature map of 16\*16\*192. By concatenating all previous layers' feature maps, the dense blocks have the comprehensive access to the extracted features which make it more robust in fusing hierarchical features sparse input, LR image in this case.

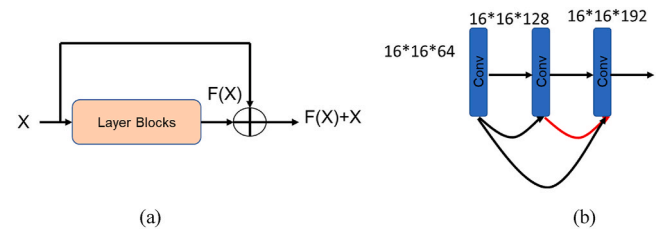
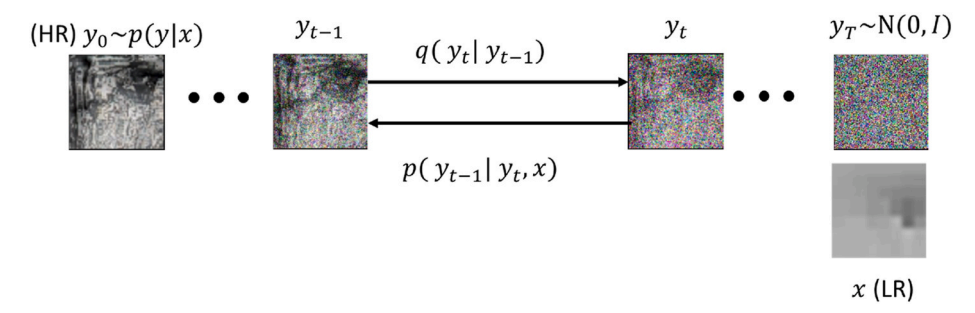


Figure A1. Residual and Dense connection (B) DDPM model.



**Figure A2.** The Diffusion probabilistic model process. The diffusion process is denoted in probabilistic distribution q, and the reverse process to retrieve the target image is denoted in probabilistic distribution p.

As shown in Figure A2, the objective of the DDPM model is to fit the probabilistic distribution which given lower resolution FPP surface topography image x, the output high resolution image  $y_0$  can be sampled through p(y|x). First, the diffusion process is conducted through gradually adding Gaussian noise to the target image, resulting in the image sampled from Gaussian distribution with 0 mean and variance of 1 at time step  $T(\mathbb{N}(0,\mathbb{I}))$ . This process can be denoted as q, and based on the assumption of Markov process which claims that the current state at time t only depends on the previous time step t-1. The probabilistic distribution of diffusion process at any time step can be calculated (Eq. (9))

$$q(y_{1:T}|y_0) = \prod_{t=1}^{T} q(y_t|y_{t-1})$$
(9)

$$q(\mathbf{y}_t|\mathbf{y}_{t-1}) = \mathbb{N}(\mathbf{y}_t|\sqrt{\alpha_t}\,\mathbf{y}_{t-1},\beta_t\mathbb{I}) \tag{10}$$

The added Gaussian noises follows the schedule of hyperparameters  $\alpha_t$  and  $\beta_t$  as specified in Eq. (10), and  $\alpha_t$  is between 0 and 1 with  $\beta_t = 1 - \alpha_t$ . The selection of the noise scheduling is essential for model performance, and linear scheduling is used for this work. Using the above Markov process distributions, the sampled noise image can be acquired through reparameterization. Specifically, the sample image  $y_t$  at time step t can be calculated using the previous time step image sample  $y_{t-1}$  with its probabilistic distribution  $q(y_t|y_{t-1})$  (Eq. (10)).

$$\mathbf{y}_{t} = \sqrt{\alpha_{t}} \mathbf{y}_{t-1} + \sqrt{\beta_{t}} \mathbf{Z}_{t}, \mathbf{Z}_{t} \sim \mathbb{N}(0, \mathbb{I})$$

$$\tag{11}$$

$$y_t = \sqrt{\alpha_t} y_{t-2} + \sqrt{1 - \alpha_t} Z_{t-1}$$

$$= \sqrt{\alpha_t \alpha_{t-1}} y_{t-2} + \sqrt{\alpha_t - \alpha_t \alpha_{t-1}} Z_{t-1} + \sqrt{1 - \alpha_t} Z_t$$

$$= \sqrt{\alpha_t \alpha_{t-1}} y_{t-2} + \sqrt{1 - \alpha_t \alpha_{t-1}} \overline{Z}, \overline{Z} \text{ is the merged distribution}$$
 (12)

$$\overline{\alpha_{t}} = \prod_{i=1}^{T} \alpha_{i} \tag{13}$$

$$\mathbf{y}_{t} = \sqrt{\overline{\alpha_{t}}} \mathbf{y}_{0} + \sqrt{1 - \overline{\alpha_{t}}} \overline{\mathbf{Z}} \tag{14}$$

As shown in Eqs. 11–14, the diffusion process can be sampled and characterized through Markov process and reparameterization through gradually adding Gaussian noise defined by hyperparameters. The diffused image at any time step can be directly acquired using the target image  $y_0$ . Using the above derived equations, the posterior probabilistic distribution  $q(y_{t-1}|y_t,y_0)$  is sampled using Eq. (15).

$$q(y_{t-1}|y_t,y_0) \sim \mathbb{N}\left(y_{t-1}\big|\mu,\sigma^2\mathbb{I}\right)\mu = \frac{\sqrt{\alpha_t}(1-\overline{\alpha}_{t-1})}{1-\overline{\alpha_t}}y_t + \frac{\sqrt{\overline{\alpha}_{t-1}}\beta_t}{1-\overline{\alpha_t}}y_0 \ \sigma^2 = \frac{1-\overline{\alpha}_{t-1}}{1-\overline{\alpha_t}}\beta_t \tag{15}$$

To reverse the diffusion process to match the target HR images, the denoising neural network is trained which takes the LR image x and the noisy target image (with added Gaussian noise)  $\tilde{y}$ . Based on Eq. (14),  $\tilde{y} = \sqrt{\overline{\alpha_i}} y_0 + \sqrt{1-\overline{\alpha_i}} \varepsilon$  where  $y_0$  is the noiseless target image and  $\varepsilon$  is noise vector sampled from standard Gaussian distribution. The objective of reverse process is to train the denoising neural network which gradually learns the distribution and noise vector.

Various experiments of model trainings are performed. The sample training loss and validation accuracy for the final best model, a DDPM-SR3 model, is shown in Figure A3 below.

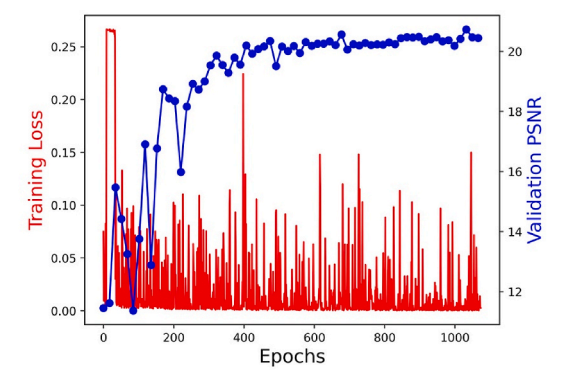


Figure A3. Training loss and validation accuracy for the final chosen DDPM-SR3 model.

#### References

- Javaid M, Haleem A. Additive manufacturing applications in medical cases: a literature based review. Alexandria Journal of Medicine 2019;54(4):411–22.
- [2] Everton SK, Hirsch M, Stravroulakis P, Leach RK, Clare AT. Review of in-situ process monitoring and in-situ metrology for metal additive manufacturing. Mater Des 2016;95:431–45.
- [3] Attaran M. The rise of 3-D printing: the advantages of additive manufacturing over traditional manufacturing. Bus Horiz 2017;60(5):677–88.
- [4] Yavari R, Smoqi Z, Riensche A, Bevans B, Kobir H, Mendoza H, et al. Part-scale thermal simulation of laser powder bed fusion using graph theory: effect of thermal history on porosity, microstructure evolution, and recoater crash. Mater Des 2021; 204-109685
- [5] Vandenbroucke B, Kruth JP. Selective laser melting of biocompatible metals for rapid manufacturing of medical parts. Rapid Prototyp J 2007;13(4):196–203.
- [6] Thanki A, Witvrouw A, Haitjema H, editors. Effect of process parameters on the surface topography formation in precision additive metal manufacturing. Euspen; Northampton: Conference Proceedings Euspen 20th Interfantional Conference & Exhibition; 2020.
- [7] Triantaphyllou A, Giusca CL, Macaulay GD, Roerig F, Hoebel M, Leach RK, et al. Surface texture measurement for additive manufacturing. Surf Topogr Metrol Prop 2015;3(2):024002.
- [8] Shi Z, Mandal S, Harimkar S, Liu C. Surface morphology analysis using convolutional autoencoder in additive manufacturing with laser engineered net shaping. Procedia Manuf 2021;53:16–23.
- [9] Leach R. Optical measurement of surface topography. Springer; 2011.
- [10] Guan G, Hirsch M, Lu ZH, Childs DT, Matcher SJ, Goodridge R, et al. Evaluation of selective laser sintering processes by optical coherence tomography. Mater Des 2015;88:837–46.
- [11] DePond PJ, Guss G, Ly S, Calta NP, Deane D, Khairallah S, et al. In situ measurements of layer roughness during laser powder bed fusion additive manufacturing using low coherence scanning interferometry. Materials & Design; 2019.
- [12] Townsend A, Senin N, Blunt L, Leach R, Taylor J. Surface texture metrology for metal additive manufacturing: a review. Precis Eng 2016;46:34–47.
- [13] Dickins A, Widjanarko T, Sims-Waterhouse D, Thompson A, Lawes S, Leach R. Multi-view fringe projection system for surface topography measurement during metal powder bed fusion. Journal of the Optical Society of America A, Optics, image science, and vision 2020;37(9):B93–105.
- [14] Zhou G, Li Z, Wang C, Shi Y. A novel method for human expression rapid reconstruction. Tsinghua Sci Technol 2009;14:62–5.
- [15] Yagnik J, Siva GS, Ramakrishnan K, Rao LK, editors. 3D shape extraction of human face in presence of facial hair: a profilometric approach. TENCON 2005-2005 IEEE region 10 conference. IEEE; 2005.
- [16] Chen L-C, Huang C-C. Miniaturized 3D surface profilometer using digital fringe projection. Meas Sci Technol 2005;16(5):1061.
- [17] High accuracy confocal full-field 3-D surface profilometry for micro lenses using a digital fringe projection strategy. In: Chen LC, Chang YW, editors. Key engineering materials. Trans Tech Publ; 2008.
- [18] Williams RJ, Davies CM, Hooper PA. In situ monitoring of the layer height in laser powder bed fusion. Mater.Des. Process. Commun. 2021;3(6):e173.
- [19] O'Dowd NM, Wachtor AJ, Todd MD. Effects of digital fringe projection operational parameters on detecting powder bed defects in additive manufacturing. Addit Manuf 2021;48.
- [20] Zhang B, Ziegert J, Farahi F, Davies A. In situ surface topography of laser powder bed fusion using fringe projection. Addit Manuf 2016;12:100-7.
- [21] Zhang H, Vallabh CKP, Xiong Y, Zhao X. A systematic study and framework of fringe projection profilometry with improved measurement performance for in-situ LPBF process monitoring. Measurement 2022:191.
- [22] Southon N, Stavroulakis P, Goodridge R, Leach R. In-process measurement and monitoring of a polymer laser sintering powder bed with fringe projection. Mater Des 2018;157:227–34.

- [23] Zhang S. Rapid and automatic optimal exposure control for digital fringe projection technique. Opt Laser Eng 2020;128:106029.
- [24] Zhang L, Chen Q, Zuo C, Feng S. High-speed high dynamic range 3D shape measurement based on deep learning. Opt Laser Eng 2020;134:106245.
- [25] Suresh V, Wang Y, Li B. High-dynamic-range 3D shape measurement utilizing the transitioning state of digital micromirror device. Opt Laser Eng 2018;107:176–81.
- [26] Feng S, Zhang L, Zuo C, Tao T, Chen Q, Gu G. High dynamic range 3D measurements with fringe projection profilometry: a review. Meas Sci Technol 2018;29(12):122001.
- [27] Liu Y, Blunt L, Gao F, Jiang X. High-dynamic-range 3D measurement for E-beam fusion additive manufacturing based on SVM intelligent fringe projection system. Surf Topogr Metrol Prop 2021;9(3):034002.
- [28] Shaheen A, Sims-Waterhouse D, Bointon P, Takushima S, Piano S, Leach RK. Characterisation of a multi-view fringe projection system based on the stereo matching of rectified phase maps. Meas Sci Technol 2021;32(4):045006.
- [29] Dickins A, Widjanarko T, Sims-Waterhouse D, Thompson A, Lawes S, Senin N, et al. Multi-view fringe projection system for surface topography measurement during metal powder bed fusion. JOSA A 2020;37(9):B93–105.
- [30] Deepc-mvs: deep confidence prediction for multi-view stereo reconstruction. In: Kuhn A, Sormann C, Rossi M, Erdler O, Fraundorfer F, editors. 2020 international conference on 3D vision (3DV). IEEE; 2020.
- [31] Pointnet: deep learning on point sets for 3d classification and segmentation. In: Qi CR, Su H, Mo K, Guibas LJ, editors. Proceedings of the IEEE conference on computer vision and pattern recognition; 2017.
- [32] End-to-end convolutional neural network for 3D reconstruction of knee bones from bi-planar X-ray images. In: Kasten Y, Doktofsky D, Kovler I, editors. International workshop on machine learning for medical image reconstruction. Springer; 2020.
- [33] Dourado CM, da Silva SPP, da Nobrega RVM, Reboucas Filho PP, Muhammad K, de Albuquerque VHC. An open IoHT-based deep learning framework for online medical image recognition. IEEE J Sel Area Commun 2020;39(2):541–8.
- [34] Deep residual learning for image recognition. In: He K, Zhang X, Ren S, Sun J, editors. Proceedings of the IEEE conference on computer vision and pattern recognition; 2016.
- [35] Liu C, Wang RR, Ho I, Kong ZJ, Williams C, Babu S, et al. Toward online layer-wise surface morphology measurement in additive manufacturing using a deep learningbased approach. J Intell Manuf 2022:1–17.
- [36] Spoorthi G, Gorthi RKSS, Gorthi S. PhaseNet 2.0: phase unwrapping of noisy data based on deep learning approach. IEEE Trans Image Process 2020;29:4862–72.
- [37] Spoorthi G, Gorthi S, Gorthi RKSS. PhaseNet: a deep convolutional neural network for two-dimensional phase unwrapping. IEEE Signal Process Lett 2018;26(1):54–8.
- [38] Zhang B, Davies A, Evans C, Ziegert J. Validity of the instrument transfer function for fringe projection metrology. Appl Opt 2018;57(11):2795–803.
- [39] Anwar S, Khan S, Barnes N. A deep journey into super-resolution. ACM Comput Surv 2020;53(3):1–34.
- [40] He K, Zhang X, Ren S, Sun J. Deep residual learning for image recognition. 2016.
  p. 770–8
- [41] Residual dense network for image super-resolution. In: Zhang Y, Tian Y, Kong Y, Zhong B, Fu Y, editors. Proceedings of the IEEE conference on computer vision and pattern recognition; 2018.
- [42] Ho J, Jain A, Abbeel P. Denoising diffusion probabilistic models. Adv Neural Inf Process Syst 2020;33:6840–51.
- [43] Nichol AQ, Dhariwal P, editors. Improved denoising diffusion probabilistic models. International Conference on Machine Learning; 2021 [PMLR].
- [44] Saharia C, Ho J, Chan W, Salimans T, Fleet DJ, Norouzi M. Image super-resolution via iterative refinement. 2021. arXiv preprint arXiv:210407636.
- [45] Zhang Z. A flexible new technique for camera calibration. IEEE Trans Pattern Anal Mach Intell 2000;22(11):1330-4.
- [46] Nakamura J. Image sensors and signal processing for digital still cameras. CRC press; 2017.
- [47] Dong C, Loy CC, He K, Tang X. Image super-resolution using deep convolutional networks. IEEE Trans Pattern Anal Mach Intell 2015;38(2):295–307.

- [48] Real-time single image and video super-resolution using an efficient sub-pixel convolutional neural network. In: Shi W, Caballero J, Huszar F, Totz J, Aitken AP, Bishop R, et al., editors. Proceedings of the IEEE conference on computer vision and pattern recognition; 2016.
- and pattern recognition; 2016.

  [49] Kingma DP, Ba J. Adam: a method for stochastic optimization. 2014. arXiv preprint arXiv:14126980.
- [50] Eastwood J, Newton L, Leach R, Piano S. Generation and categorisation of surface texture data using a modified progressively growing adversarial network. Precis Eng 2022;74:1–11.
- [51] Zhang P, Zhong K, Li Z, Zhang B. Hybrid-quality-guided phase fusion model for high dynamic range 3D surface measurement by structured light technology. Opt Express 2022;30(9):14600–14.